The Institution of
Engineering and Technology

ORIGINAL RESEARCH OPEN ACCESS

An Improved Rotor Flux Observer-Based Sensorless Control Method for Dual Three-Phase Axial Flux PMSM

Anchen Yang[1] | Mingyao Lin[1] | Yixiang Tu[1] | Lun Jia[1] | Keman Lin[2] | Peng Wang[3]

[1]School of Electrical Engineering, Southeast University, Nanjing, China | [2]College of Electrical and Power Engineering, Hohai University, Nanjing, China | [3]Department of Electronic and Electrical Engineering, University of Sheffield, Sheffield, UK

Correspondence: Mingyao Lin (mylin@seu.edu.cn)

ABSTRACT

Due to the remarkable performance, dual three-phase axial flux permanent magnet synchronous motors (DTP-AFPMSMs) are increasingly being adopted in the field of electric vehicles (EVs). However, the installation of position sensors limits the application scenarios of DTP-AFPMSMs owing to increased complexity, size and cost. This article proposes an innovative high-speed sensorless control method for surface-mounted DTP-AFPMSMs using an improved rotor flux observer. The proposed observer achieves precise rotor flux estimation by filtering out harmonic distortion and noise from the rotor flux of the first winding set using high-pass and low-pass filters, followed by a tracking-mode PI controller that accurately tracks the phase and amplitude of the rotor flux in the second winding set. Therefore, the proposed method can enable accurate rotor position estimation without the need for a phase-locked loop (PLL) and realise a more precise sensorless motor control. A series of simulations and experiments are carried out to validate the effectiveness of the observer, which reveals that the proposed method can effectively estimate the electrical position angle with a tiny error and presents a considerable improvement over the conventional method.

1 | Introduction

In recent years, dual three-phase permanent magnetic synchronous motors (DTP-PMSMs) have gained significant recognition for numerous advantages, including high fault tolerance [1], the ability to deliver high power even at low voltages and minimised torque ripple [2]. DTP-PMSMs, also known as asymmetric six-phase motors, represent one of two distinct configurations within six-phase motors. Six-phase motors consist of symmetric six-phase (with $\pi/3$ electrical radians shift) and asymmetric six-phase (with $\pi/6$ electrical radians shift) motors. Symmetric six-phase motors maintain a $\pi/3$ electrical radians phase belt angle identical to three-phase motors, whereas asymmetric

six-phase motors employ a $\pi/6$ electrical radians phase belt angle that effectively eliminates 5th and 7th harmonic magnetomotive forces. Hence, the 6th order torque pulsation of DTP-PMSMs is eliminated. These characteristics make DTP-PMSMs particularly very suitable for electric vehicle (EV) applications, where reliable and efficient motor operation is essential [3]. The motor configuration with $\pi/6$ electrical radians shift is adopted in this work. Each stator winding set has its own isolated neutral point [4]. This design allows for enhanced control flexibility and improved fault tolerance, as each winding set of DTP-PMSMs can be operated independently. When the leakage inductance between the winding sets is negligible, the motor can be modelled as two coupled three-phase PMSMs with identical

parameters [2]. Consequently, the control methods developed for the conventional three-phase PMSMs can be adapted and applied to DTP-PMSMs with slight modifications [5].

Axial flux permanent magnet synchronous motors (AFPMSMs) are appreciated for their compact design, high efficiency and high-power density. Unlike conventional radial flux motors, AFPMSMs reduce the volume of motors without compromising performance. Thus, the AFPMSM benefits occasions requiring efficient space utilisation and high performance. Building on the characteristics of AFPMSMs, dual three-phase AFPMSMs (DTP-AFPMSMs) merge the strengths of both structures, offering enhanced control capabilities and even higher performance for applications such as EVs.

For optimal control of DTP-AFPMSMs in EVs, accurate rotor position information is crucial [6]. Traditionally, high-resolution position sensors such as encoders or resolvers are mounted on the motor shaft to provide this information. Although these sensors can provide reliable and accurate position information, several drawbacks will also be introduced by using position sensors. Firstly, installing high-resolution position sensors increases the overall cost of the system. Additionally, these sensors will add to both system complexity and physical size [7]. Moreover, the position sensors installed on the motor will limit the applicability of DTP-AFPMSMs in environments where space and cost constraints are critical [8]. These challenges have put forward the demand for the development of sensorless control algorithms [9, 10], which can eliminate the requirement for physical sensors while maintaining or even improving motor control performance.

Commonly, sensorless control strategies can be classified into back-EMF-based methods for medium and high-speed operations, and high-frequency signal injection techniques for low and zero speeds where back-EMF is insufficient. Numerous signal injection-based sensorless methods have been proposed in recent years [11–13]. In conventional high-speed sensorless control algorithms, a phase-lock loop (PLL) [14] is often combined with back electromotive force observers [15–17], sliding-mode observers [18–21] or linear state observers to ensure stable frequency output while compensating for input signal variations and system disturbances. Traditional PLL-based methods suffer from inherent phase lag during dynamic operations and poor noise immunity, which will cause steady-state position estimation errors [11]. Additionally, the efficiency of the system will be reduced. If the rotor fluxes are sufficiently accurate to allow stable and precise position acquisition only through Arctan calculations, the PLL can be eliminated, so the control algorithm can be simplified and the system efficiency can be enhanced.

Consequently, an improved rotor flux observer specifically is designed for DTP-AFPMSMs. The improved rotor flux observer is based on a well-known active flux observer designed for three-phase PMSM [22–26]. The rotor position is accurately determined without relying on a PLL in the presented method. Unlike conventional methods, the proposed observer eliminates PLL dependency while effectively reducing harmonic distortion, phase lag and amplitude attenuation. Due to the mathematical model of DTP-AFPMSMs being identical to that of radial flux

surface-mounted DTP-PMSMs, the proposed method can also be applied to radial flux motors. However, the algorithm is specifically designed for surface-mounted DTP-PMSMs; it is not applicable to single three-phase PMSMs or interior PMSMs. Numerous simulations and experiments have been conducted to validate the effectiveness and superiority of the proposed method. The proposed method is particularly well-suited for DTP-AFPMSMs, making it an ideal option for various applications, particularly in EVs.

The structure of this paper is organised as follows: Section 2 introduces the improved rotor flux observer, explaining its design and operational principles, with a focus on addressing key challenges such as amplitude attenuation, phase lag, and harmonic distortion. Section 3 details the tests conducted to validate the method, demonstrating the accuracy and reliability of the observer under various operating conditions. Finally, Section 4 presents the conclusion.

2 | Improved Flux Observer-Based Sensorless Algorithm

2.1 | Analytical Model for DTP-AFPMSM Based on Double dq Model

The stator voltage equation of a DTP-AFPMSM based on double dq model [27] can be expressed as follows:

$$\begin{cases} u_{d1} = Ri_{d1} + \dfrac{d}{dt}(L_d i_{d1} + L_{dd} i_{d2}) - \omega_e(L_q i_{q1} + L_{qq} i_{q2}) \\ u_{q1} = Ri_{q1} + \dfrac{d}{dt}(L_q i_{q1} + L_{qq} i_{q2}) + \omega_e\left(L_d i_{d1} + L_{dd} i_{d2} + \psi_f\right) \\ u_{d2} = Ri_{d2} + \dfrac{d}{dt}(L_{dd} i_{d1} + L_d i_{d2}) - \omega_e(L_{qq} i_{q1} + L_q i_{q2}) \\ u_{q2} = Ri_{q2} + \dfrac{d}{dt}(L_{qq} i_{q1} + L_q i_{q2}) + \omega_e\left(L_{dd} i_{d1} + L_d i_{d2} + \psi_f\right) \end{cases}, \quad (1)$$

where ψ_f represents the value of the rotor flux, which is equal to the PM flux. i_{d1}, i_{q1}, i_{d2}, i_{q2}, u_{d1}, u_{q1}, u_{d2}, and u_{q2} denote the current and voltage in the double dq-axes, respectively. The stator inductances for the two winding sets in the dq-axis are denoted as L_{dd}, L_{qq}, L_d, and L_q, respectively [28]. R refers to the phase resistance of the DTP-AFPMSM. Finally, ω_e is the electrical angular velocity.

The difference between the stator inductances of two sets of windings is the leakage inductance L_z of the DTP-AFPMSM, which could be expressed as follows:

$$\begin{cases} L_d = L_{dd} + L_z, \\ L_q = L_{qq} + L_z, \end{cases} \quad (2)$$

where L_z represents the leakage inductance of the DTP-AFPMSM.

In the calculation of rotor and stator fluxes, L_z is significantly smaller than the stator inductances and can therefore be disregarded. As the motor utilised in this article is a surface-mounted PMSM, the stator inductances in the dq-axis are

equal. Consequently, it can be inferred that the stator inductance can be expressed as follows:

$$L = L_d = L_{dd} = L_q = L_{qq}. \tag{3}$$

Hence, the stator flux equations of the two winding sets in the $\alpha\beta$-axes, derived from the double dq model [29], can be formulated as follows [30]:

$$\begin{cases} \psi_{\alpha 1} = 2i_{\alpha 1}L + \psi_{f\alpha 1} \\ \psi_{\beta 1} = 2i_{\beta 1}L + \psi_{f\beta 1} \\ \psi_{\alpha 2} = 2i_{\alpha 2}L + \psi_{f\alpha 2} \\ \psi_{\beta 2} = 2i_{\beta 2}L + \psi_{f\beta 2} \end{cases}, \tag{4}$$

in which $\psi_{\alpha 1}$, $\psi_{\beta 1}$, $\psi_{\alpha 2}$, and $\psi_{\beta 2}$ represent the stator fluxes of double $\alpha\beta$-axes, respectively. $\psi_{f\alpha 1}$, $\psi_{f\beta 1}$, $\psi_{f\alpha 2}$, and $\psi_{f\beta 2}$ denote the rotor fluxes of double $\alpha\beta$-axes, respectively. $i_{\alpha 1}$, $i_{\beta 1}$, $i_{\alpha 2}$, and $i_{\beta 2}$ are the currents of two winding sets in two $\alpha\beta$-axes, respectively.

Derived from the double dq model in the $\alpha\beta$-axes, the stator voltage equations for both winding sets are established, which can be expressed as follows:

$$\begin{cases} u_{\alpha 1} = i_{\alpha 1}R + \dfrac{d}{dt}\psi_{\alpha 1} \\[2mm] u_{\beta 1} = i_{\beta 1}R + \dfrac{d}{dt}\psi_{\beta 1} \\[2mm] u_{\alpha 2} = i_{\alpha 2}R + \dfrac{d}{dt}\psi_{\alpha 2} \\[2mm] u_{\beta 2} = i_{\beta 2}R + \dfrac{d}{dt}\psi_{\beta 2} \end{cases}, \tag{5}$$

in which $u_{\alpha 1}$, $u_{\beta 1}$, $u_{\alpha 2}$, and $u_{\beta 2}$ represent the voltages of two winding sets in two $\alpha\beta$-axes, respectively. From Equation (5), it is evident that the voltage equations for the two winding sets are nearly identical. The only distinction is the position angle used in coordinate transformation. Therefore, the PM fluxes of double $\alpha\beta$-axis, which exhibit identical waveforms with a phase shift of $\pi/6$, can be formulated as follows:

$$\begin{cases} \psi_{f\alpha 1} = \dfrac{1}{s}(u_{\alpha 1} - i_{\alpha 1}R) - 2i_{\alpha 1}L \\[2mm] \psi_{f\beta 1} = \dfrac{1}{s}(u_{\beta 1} - i_{\beta 1}R) - 2i_{\beta 1}L \\[2mm] \psi_{f\alpha 2} = \dfrac{1}{s}(u_{\alpha 2} - i_{\alpha 2}R) - 2i_{\alpha 2}L \\[2mm] \psi_{f\beta 2} = \dfrac{1}{s}(u_{\beta 2} - i_{\beta 2}R) - 2i_{\beta 2}L \end{cases}. \tag{6}$$

The rotor position is calculable from the rotor fluxes, and the relationship could be obtained as follows:

$$\theta_e = \arctan\frac{\psi_{f\beta 1}}{\psi_{f\alpha 1}} = \arctan\frac{\psi_{f\beta 2}}{\psi_{f\alpha 2}} - \frac{\pi}{6}, \tag{7}$$

Because the PM fluxes of the 2nd winding set, $\psi_{f\alpha 2}$ and $\psi_{f\beta 2}$ are phase-shifted by $\pi/6$ electrical radian relative to the 1st set, the PM fluxes of the 1st winding set could be computed as follows:

$$\begin{cases} \tilde{\psi}_{f\alpha 1} = \psi_{f\alpha 2}\cos\dfrac{\pi}{6} + \psi_{f\beta 2}\sin\dfrac{\pi}{6} \\[2mm] \tilde{\psi}_{f\beta 1} = \psi_{f\beta 2}\cos\dfrac{\pi}{6} - \psi_{f\alpha 2}\sin\dfrac{\pi}{6} \end{cases}, \tag{8}$$

in which $\tilde{\psi}_{f\alpha 1}$ and $\tilde{\psi}_{f\beta 1}$ represent the calculated results of rotor fluxes of the 1st winding set in $\alpha\beta$-axes, respectively.

2.2 | Design of Improved Observer

It can be seen from Equation (6) that the direct calculation of PM fluxes from measured voltages and currents is confronted with challenges such as high-frequency noise and DC bias. These factors undermine the accuracy and reliability of flux calculation, particularly when used to obtain rotor position directly. Only high-precision rotor fluxes, addressing the issues mentioned, can be utilised for the direct calculation of position angles without PLL. An improved method has been introduced to enhance the sensorless performance of DTP-AFPMSM by obtaining rotor fluxes more accurately.

Figure 1 shows the block diagram of the proposed sensorless method for DTP-AFPMSM, and Figure 2 illustrates its structure. The position angle is calculated through the observation of the PM fluxes from the 1st set of windings. For the avoidance of DC bias, a high-pass filter (HPF) G_1 is employed following the integrator. Additionally, a low-pass filter (LPF) G_2 is utilised following the output of PM fluxes to diminish the impact of high-frequency noise.

After using two filters, the rotor flux waveforms become smoother, but at the cost of reduced amplitude and delayed phase. Hence, a correction of the observed rotor fluxes is deemed necessary.

For the DTP-AFPMSM, it is noted that the PM fluxes in the 2nd winding set contain the position information as well. In the absence of filtering, $\psi_{f\alpha\beta 2}$ exhibit significant noise but retain the exact phase and amplitude. To eliminate amplitude and phase errors, a tracking-mode PI controller is implemented as feedback.

The transfer function of the observed rotor fluxes $\hat{\psi}_{f\alpha\beta 1}$ can be expressed as follows:

$$\hat{\psi}_{f\alpha\beta 1} = \left[\frac{1}{s}(u_{\alpha\beta 1} - Ri_{\alpha\beta 1} - D_{\alpha\beta 1})\frac{s}{s+\omega_1} - 2i_{\alpha\beta 1}L\right]\frac{\omega_2}{s+\omega_2}, \tag{9}$$

in which $D_{\alpha\beta 1}$ are the feedback errors in $\alpha\beta$-axes, respectively. ω_1 and ω_2 are the cut-off frequency of the HPF G_1 and the LPF G_2, respectively.

$$\begin{aligned} D_{\alpha\beta 1} = k_p\left(\hat{\psi}_{f\alpha\beta 1} - \tilde{\psi}_{f\alpha\beta 1}\right) + \frac{1}{s}\Big[k_i\left(\hat{\psi}_{f\alpha\beta 1} - \tilde{\psi}_{f\alpha\beta 1}\right) \\ + k_t\left(\tilde{\psi}_{f\alpha\beta 1} - D_{\alpha\beta 1}\right)\Big]. \end{aligned} \tag{10}$$

The feedback error's transfer function could be presented as Equation (10), where k_p, k_i, and k_t are the proportional,
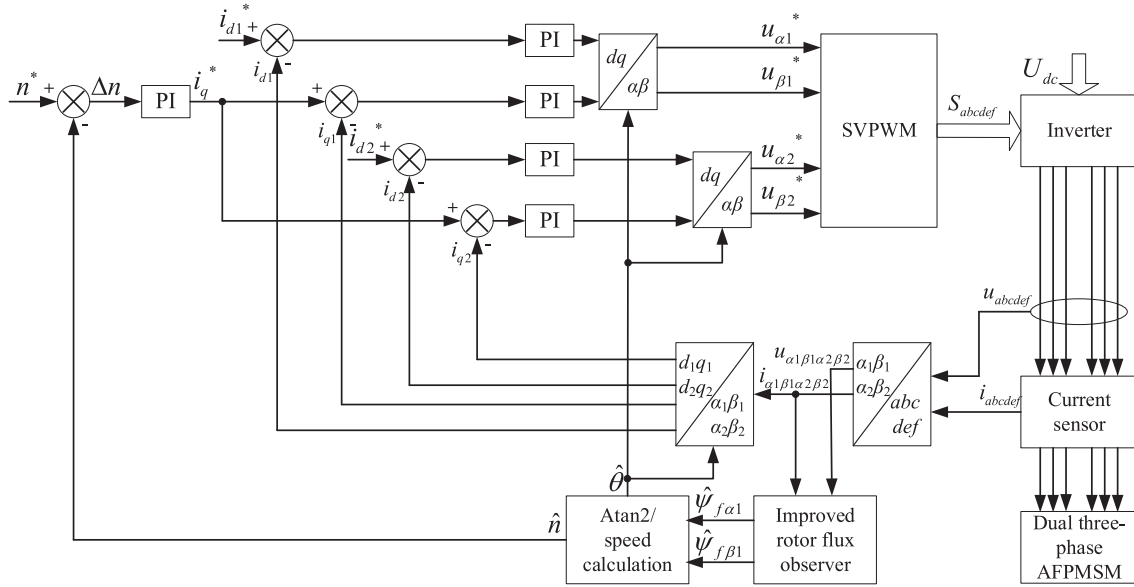
FIGURE 1 | Block diagram of the proposed sensorless control system.

integral, and tracking parameters of the feedback controller, respectively.

Upon rearranging Equation (10), the feedback error's transfer function could be reformulated as follows:

than its denominator order. This characteristic ensures the attenuation of high-frequency components. Therefore, the transfer function demonstrates that the proposed observer can suppress the effects caused by inductance parameter error, exhibiting disturbance rejection capabilities.

$$\hat{\psi}_{f\alpha\beta1} = \left[\left(u_{\alpha\beta1} - Ri_{\alpha\beta1} - \frac{sk_p + k_i}{s + k_t}\hat{\psi}_{f\alpha\beta1} - \frac{-sk_p - k_i + k_t}{s + k_t}\tilde{\psi}_{f\alpha\beta1}\right)\frac{1}{s + \omega_1} - 2i_{\alpha\beta1}L\right]\frac{\omega_2}{s + \omega_2}, \tag{12}$$

$$\hat{\psi}_{f\alpha\beta1} = \frac{\omega_2(s + k_t)u_{\alpha\beta1} - \omega_2(s + k_t)[R + 2(s + \omega_1)L]i_{\alpha\beta1} - \omega_2(-sk_p - k_i + k_t)\tilde{\psi}_{f\alpha\beta1}}{s^3 + (\omega_1 + \omega_2 + k_t)s^2 + (\omega_1 k_t + \omega_2 k_t + \omega_1\omega_2 + \omega_2 k_p)s + (\omega_1\omega_2 k_t + \omega_2 k_i)}, \tag{13}$$

$$\hat{\psi}_{f\alpha\beta1\text{err}}(\Delta L) = \hat{\psi}_{f\alpha\beta1} - \frac{2\omega_2(s^2 + s(k_p + k_t + \omega_1) + k_t\omega_1 + k_i - k_t)i_{\alpha\beta1}}{(s + k_t)(s + \omega_1)(s + \omega_2)}\Delta L, \tag{14}$$

$$D_{\alpha\beta1}(s) = \frac{sk_p + k_i}{s + k_t}\hat{\psi}_{f\alpha\beta1} + \frac{-sk_p - k_i + k_t}{s + k_t}\tilde{\psi}_{f\alpha\beta1}, \tag{11}$$

By substituting Equation (11) into Equation (9), the resultant transfer function of $\hat{\psi}_{f\alpha\beta1}$ would be Equation (12).

Upon rearranging Equation (12), the transfer function of observed rotor fluxes $\hat{\psi}_{f\alpha\beta1}$ could be reformulated as Equation (13).

When interferences exist among parameters, such as inductance L, it can be represented as $L + \Delta L$, where ΔL denotes the inductance error. The transfer functions between the observed and real PM fluxes are formulated in Equation (14). Analysis reveals that the transfer function preceding ΔL behaves as a low-pass filter, as its numerator order is lower

$$d(s) = s^3 + (\omega_1 + \omega_2 + k_t)s^2 + (\omega_1 k_t + \omega_2 k_t + \omega_1\omega_2 + \omega_2 k_p)s + \omega_2(\omega_1 k_t + k_i). \tag{15}$$

The output PM fluxes are devoid of phase lag and attenuation and are rendered smoothly, thereby facilitating direct calculation of the position. Consequently, the electrical position could be determined through Arctan calculation, allowing the PLL to be eliminated.

2.3 | Stability Analysis

To further ensure the performance and stability of the proposed observer, it is essential to rigorously analyse its reliability using the Routh stability criterion. The characteristic equations of the
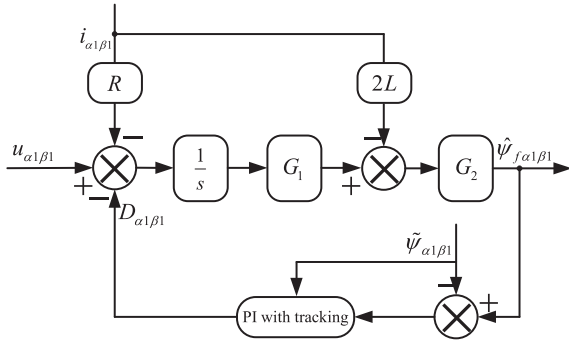
FIGURE 2 | Structure diagram of the improved flux observer.

observer, which are derived from Equation (13), can be expressed as Equation (15).

By applying the Routh stability criterion [24], it can be determined that the stability of the observer is guaranteed if all elements in the first column of the Routh array are strictly positive. The Routh array is constructed based on the characteristic polynomial of the observer, and the array is analysed to confirm the necessary conditions for stability, which is presented as follows:

$$
\begin{array}{c|cc}
s^3 & 1 & (\omega_1 k_t + \omega_2 k_t + \omega_1 \omega_2 + \omega_2 k_p) \\
s^2 & (\omega_1 + \omega_2 + k_t) & \omega_2(\omega_1 k_t + k_i) \\
s^1 & b_1 & 0 \\
s^\circ & \omega_2(\omega_1 k_t + k_i) & 0
\end{array} \quad . \tag{16}
$$

In particular, the elements in the first column of the Routh array remain positive when all system parameters exhibit positive gains. The only exception to this is the 1st-order characteristic polynomial b_1, which can be rewritten as Equation (17). From Equation (17), it can be deduced that specific parameters, namely ω_1, ω_2, k_p, k_t, $(k_p k_t - k_i)$, and $(\omega_1 k_t + k_i)$, must all be positive to maintain the stability of the system.

By setting k_i as 0, while keeping the remaining parameters positive, the stability of the observer is preserved.

simulated and experimental results. The parameters of the motor used for the simulations and experiments are listed in Table 1. The motor parameters were obtained through experimental measurements, which show good consistency with finite element analysis (FEA) simulation results using ANSYS Maxwell. The inductance analysis indicates no obvious saturation effects within the rated operating range.
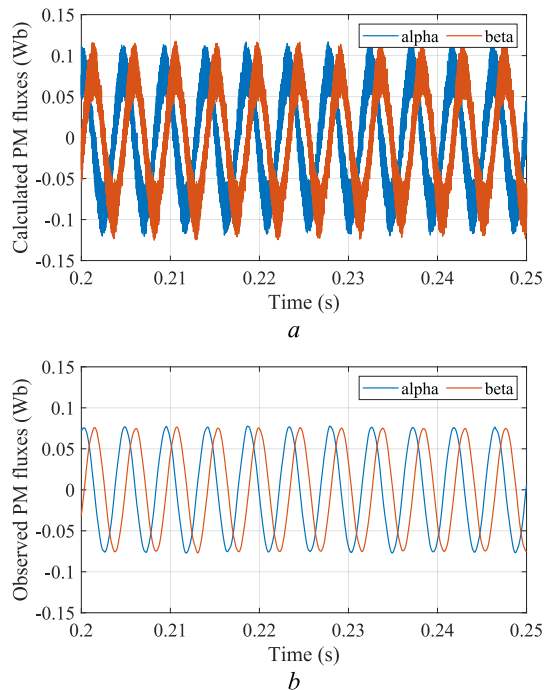
3.1 | Simulation Results

A MATLAB/Simulink model of the sensorless DTP-AFPMSM control system is built for simulation. In the simulation, the steady-state rotor speed is 1000 rpm, with the motor operating at light load and rated load. The performance of the proposed rotor flux observer is evaluated by comparing the observed rotor fluxes with those obtained through direct calculation, as shown in Figure 3. The observed rotor fluxes exhibit a smooth, sinusoidal waveform, are in quadrature, and maintain the same amplitude and phase as the fluxes derived from direct calculation. Additionally, the high-frequency noise and DC biases typically presented in direct calculations are effectively suppressed in the observed results, ensuring that the rotor fluxes are reliable and precise for position calculation. Simulation results shown in Figure 4a demonstrate that even with a substantial inductance error ($L_{err} = 0.5L$), the proposed method maintains stable flux amplitude and phase characteristics, exhibiting only minimal waveform distortion despite the 50% parameter mismatch. In contrast, Figure 4b reveals that the conventional method suffers from significant amplitude variations under the same parameter error conditions. Figures 5 and 6 further validates the accuracy of the proposed method by comparing the estimated rotor position with the real position recorded by a sensor. The close alignment between the estimated and actual positions features the accuracy of the proposed method, with a maximum position error of approximately 0.012 rad at light load and 0.008 rad at rated load. This demonstrates the

$$
b_1 = \frac{\omega_1^2 k_t + \omega_1 k_t^2 + 2\omega_1 \omega_2 k_t + \omega_2^2 k_t + \omega_2 k_t^2 + \omega_1^2 \omega_2 + \omega_1 \omega_2^2 + \omega_1 \omega_2 k_p + \omega_2^2 k_p + \omega_2(k_p k_t - k_i)}{(\omega_1 + \omega_2 + k_t)}. \tag{17}
$$

This condition is crucial because it simplifies the control strategy while ensuring that the observer operates within stable bounds. Additionally, the proposed method highlights that the parameters k_p and k_t, and the cut-off frequencies ω_1 and ω_2 can be freely tuned without compromising the stability of the observer. It offers a significant advantage in optimising the control performance without risking instability in the system. It can also be concluded that the proposed observer is stable across a wide range of operating conditions.

3 | Simulation and Experimental Results

To verify the improved rotor flux observer-based sensorless DTP-AFPMSM control system, this section presents the

capability of the proposed method to deliver high-precision sensorless position estimation in real-time operation. In Figure 7, the estimated rotor speed is compared with the actual speed measured by the sensor. The estimated speed closely follows the actual speed with minimal deviation and shows a small ripple of less than 8 rpm at light or rated load. Additionally, when the inductance has a significant error ($L_{err} = 0.5L$), the simulation results in Figure 8 show the position estimation error with the proposed method only increases slightly from 0.012 to 0.018 rad. These results further confirm the robustness of the proposed algorithm, which consistently provides reliable speed estimation. Overall, the simulation results validate both the accuracy and the practicability of the improved rotor flux observer for sensorless control of DTP-AFPMSMs.

TABLE 1 | Parameters of DTP-AFPMSM.

| Symbol	Denotation	Value
U_R	Rated voltage (V)	150
I_R	Rated current (A)	4.5
T_R	Rated torque (N·m)	12
P_R	Rated power (W)	2000
n_p	Number of pole pairs	13
R	Stator resistance (Ω)	0.56
L	Stator inductance (mH)	10.625
ψ_f	Permanent flux linkage (Wb)	0.0756

FIGURE 3 | Comparison between observed and calculated PM fluxes at light load. (a) Simulated PM fluxes by direct calculation and (b) simulated PM fluxes by proposed method.

3.2 | Experimental Results

The experimental system configuration is shown in Figure 9. The controller of the experiment is based on DSP TMS320 F28379D and runs at a 200 MHz clock frequency. The prototype of the DTP-AFPMSM is powered by a 150 V DC bus, accompanied by two three-phase IPMs switching at 10 kHz. An absolute encoder, with a resolution of 23 bits, is employed to detect the actual speed and position. The parameters of the DTP-AFPMSM used in the experiment match those used in the simulation.

Four experiments are conducted to validate the effectiveness of the proposed sensorless control method for the DTP-AFPMSM control system. In the first experiment, the motor operates at a steady-state rotor speed of 500 rpm at no load with the proposed sensorless method for position acquisition. The full absolute encoder is used only for comparison purposes. The PM
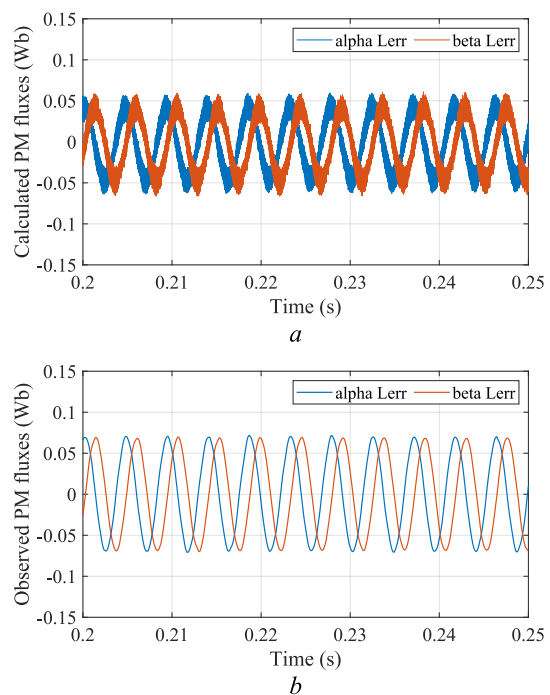

FIGURE 4 | Comparison between observed and calculated PM fluxes at light load with inductance parameter error ($L_{err} = 0.5L$). (a) Simulated PM fluxes by direct calculation and (b) simulated PM fluxes by proposed method.
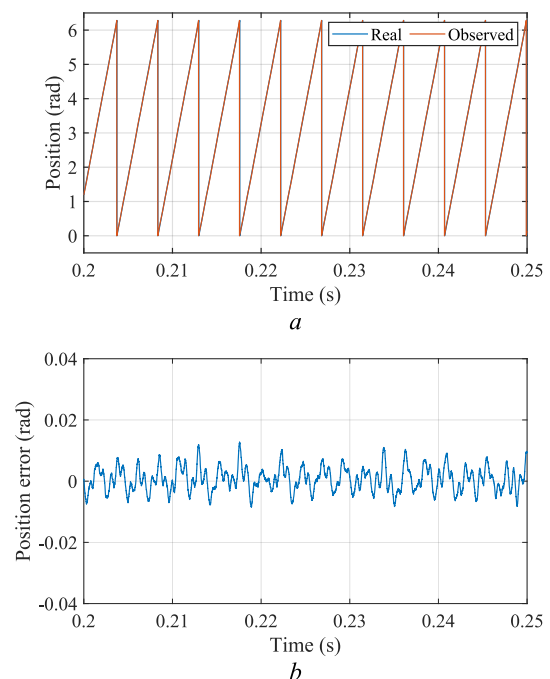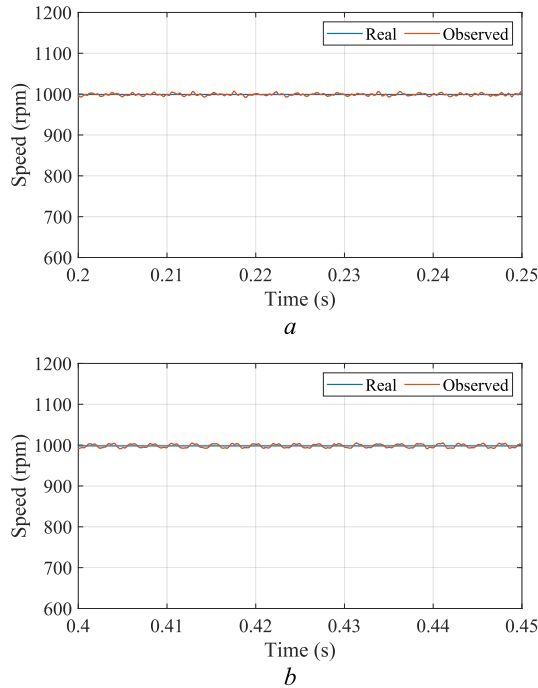

FIGURE 5 | Simulation results of the proposed sensorless method at light load. (a) Comparison between real and observed electrical positions and (b) observed position error.

fluxes generated by the proposed method at no load are shown in Figure 10a. The observed rotor fluxes are both in quadrature and smooth, and they can reliably serve as inputs for position calculation. The observed and reference speed at no load is exhibited in Figure 10b. The observed speed by the sensorless
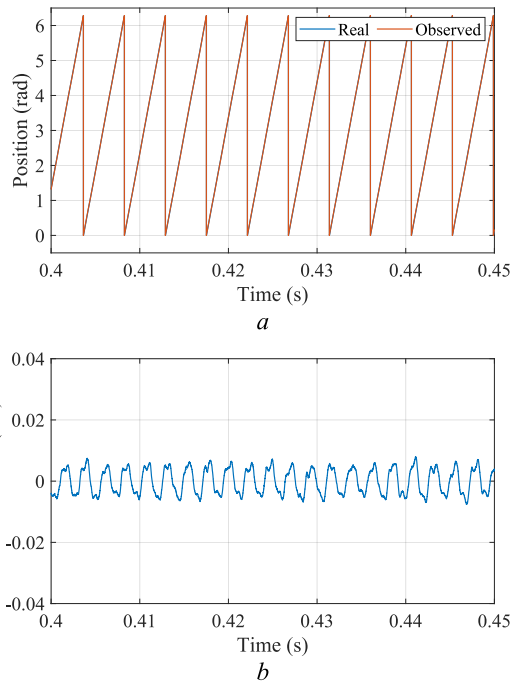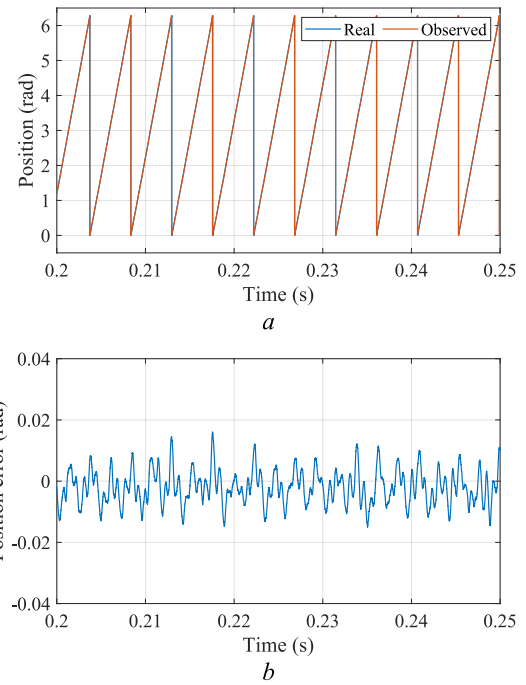
FIGURE 6 | Simulation results of the proposed sensorless method at rated load. (a) Comparison between real and observed electrical positions and (b) observed position error.
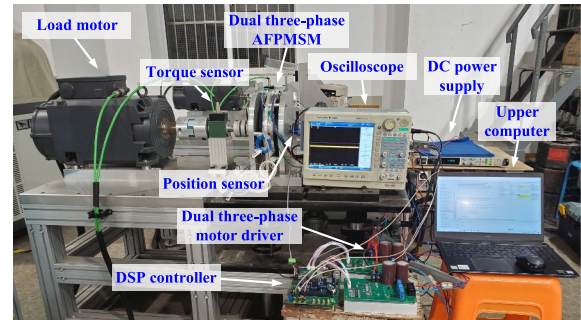

FIGURE 7 | Simulation results of comparison between real and observed speed. (a) at light load and (b) at rated load.

FIGURE 8 | Simulation results of the proposed sensorless method at light load with inductance parameter error ($L_{err} = 0.5L$). (a) Comparison between real and observed electrical positions and (b) observed position error.


FIGURE 9 | Experimental setup.

algorithm can reach the reference speed with a tiny steady error of 0.4%. Figure 11a compares the observed position from the sensorless algorithm with the real position measured by the full absolute encoder at no-load conditions, whereas Figure 11b displays the corresponding position error. The waveform of position obtained using the proposed method closely matches that of the 23-bit high-resolution full absolute encoder. The
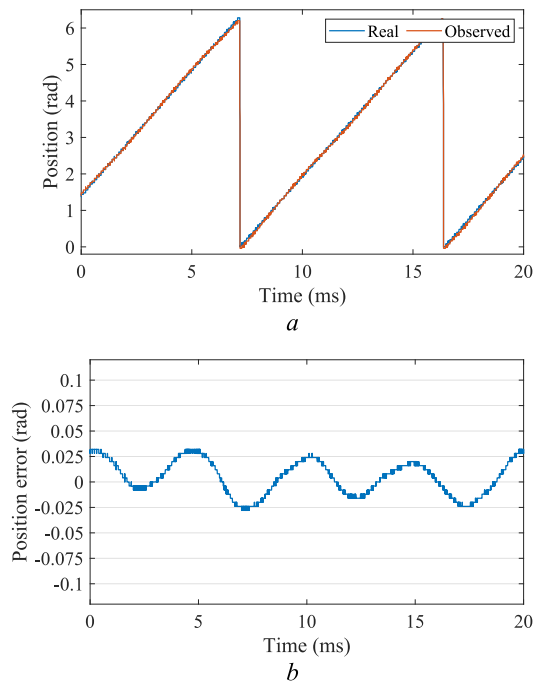
maximum position steady error is observed to be within 0.030 rad.

The second experiment maintains identical operating conditions but under heavy load. The PM fluxes generated by the proposed method at heavy load are shown in Figure 12a, which are also satisfying. The observed and reference speed at heavy load is exhibited in Figure 12b, with a tiny steady error of 0.6%. The position estimation performance is illustrated in Figure 13, where the maximum steady-state error between observed and real positions remains within 0.025 rad.

The third experiment replicates the conditions of the first experiment but introduces a significant inductance error ($L_{err} = 0.5L$). Figure 14a demonstrates that the proposed method maintains robust flux estimation with consistent amplitude and phase characteristics despite the parameter variation. As shown in Figure 14b, the position estimation error increases only slightly from 0.030 to 0.040 rad under this severe parameter mismatch.
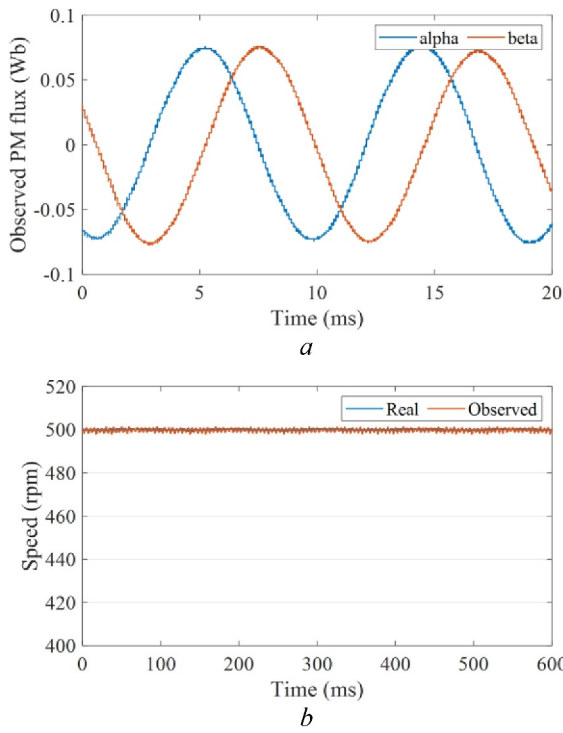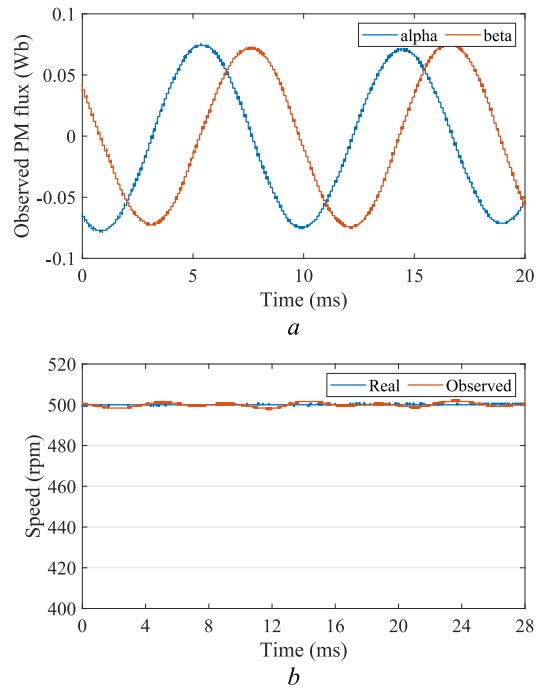
FIGURE 10 | Experimental results of observed PM fluxes and rotor speed at no load. (a) Observed two-phase PM fluxes and (b) comparison between reference and observed rotor speed.

FIGURE 12 | Experimental results of observed PM fluxes and rotor speed at heavy load. (a) Observed two-phase PM fluxes and (b) comparison between reference and observed rotor speed.
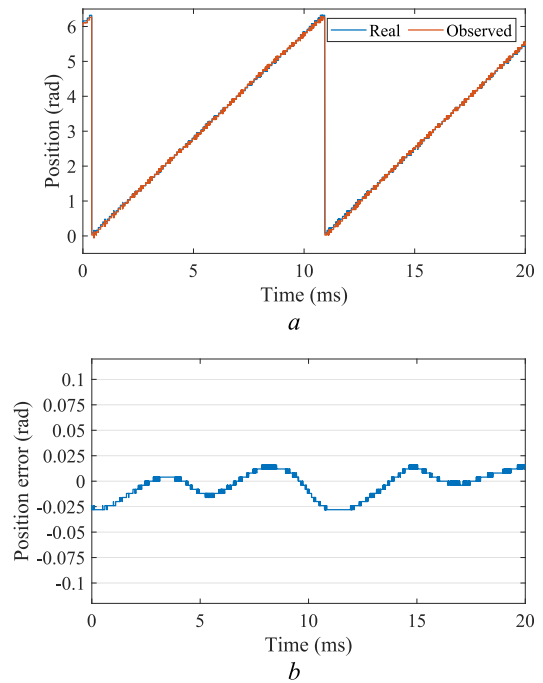

FIGURE 11 | Experimental results of electrical position angle at no load. (a) Comparison between real and observed electrical position angle and (b) position error between real and observed electrical position angle.

FIGURE 13 | Experimental results of electrical position angle at heavy load. (a) Comparison between real and observed electrical position angle and (b) position error between real and observed electrical position angle.

The fourth experiment involves comparing the different PM flux calculation methods during the steady-state operation. Figure 15a illustrates the comparison between the PM flux generated by the improved rotor flux observer and that obtained by direct calculation. The comparison reveals that the PM fluxes generated by each method possess similar amplitude and phase. However, the waveform of the PM flux by calculation is not sinusoidal and exhibits noticeable distortion. The THD analysis results of the PM fluxes are shown in Table 2. The harmonics
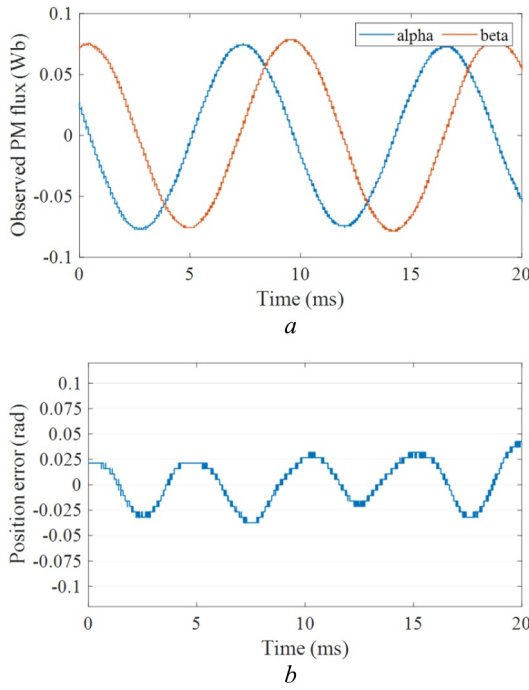
FIGURE 14 | Experimental results with inductance parameter error (L_{err} = 0.5L). (a) Observed PM fluxes and (b) position error between real and observed electrical position angle.
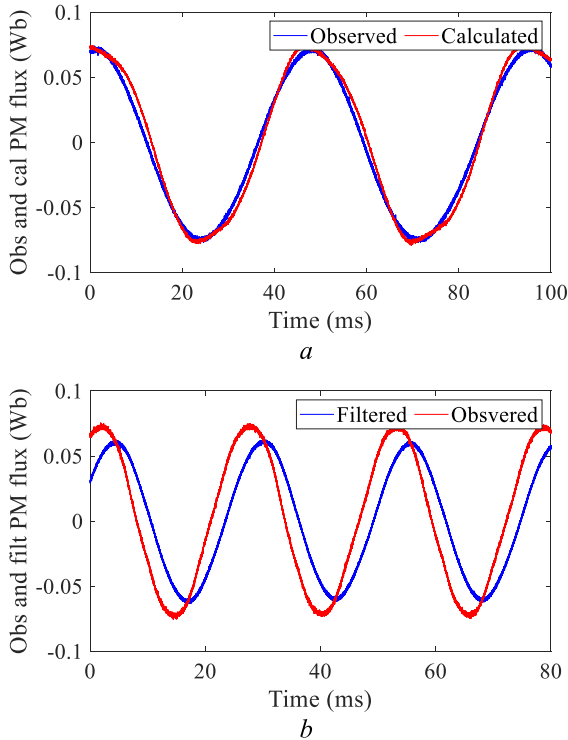
FIGURE 15 | Experimental results of PM flux comparison. (a) Comparison between observed and calculated PM flux and (b) comparison between observed and filtered PM flux.

higher than the 6th order are relatively small, so the table has ignored it. The observed PM flux only has 2.67% of THD while the calculated PM flux has 9.99%. When utilising the calculated result for obtaining the rotor position, the maximum position

TABLE 2 | THD analysis of PM fluxes.

Frequency (Hz)/order	Percentage (%)	Phase
Observed		
0 (DC)	2.05	270.0°
21.6667 (Fnd)	100.00	232.7°
43.3333 (h2)	2.03	−86.5°
65 (h3)	0.69	219.0°
86.6667 (h4)	1.01	211.5°
108.333 (h5)	0.42	144.7°
130 (h6)	0.39	177.1°
Calculated		
0 (DC)	4.31	270.0°
21.6667 (Fnd)	100.00	20.7°
43.3333 (h2)	4.21	−3.6°
65 (h3)	8.63	9.0°
86.6667 (h4)	1.20	34.0°
108.333 (h5)	0.80	−59.8°
130 (h6)	0.92	0.2°

steady error can be up to 0.250 rad, so the accuracy cannot be guaranteed. Figure 15b presents the comparison between the PM flux generated by the improved rotor flux observer and that generated simply using low-pass and high-pass filters. From the comparison, it can be concluded that the PM fluxes generated by each method are both sinusoidal. Nevertheless, the waveform of the PM flux obtained by using filters clearly demonstrates amplitude attenuation and phase lag. When the filtered result is used to obtain the rotor position, amplitude attenuation might not pose significant issues, as the amplitudes of the two-phase PM fluxes are attenuated simultaneously, but the phase lag will still exist in the result of the rotor position. In fact, the phase lag can reach up to 0.7 rad at a speed of 100 rpm. As a result, neither directly calculating the PM fluxes nor using filters alone is suitable for acquiring the rotor position. The introduction of the improved rotor flux observer is necessary and of great benefit.

4 | Conclusion

A novel sensorless control method for DTP-AFPMSMs, which utilises an improved rotor flux observer, has been presented in this article. The innovative observer design allows for accurate rotor flux acquisition without amplitude attenuation, phase lag and significant harmonic distortion. The design of the proposed method in dual $\alpha\beta$-axes also allows for the calculation of sampled voltages and currents without requiring position information for coordinate transformation. The high-precision observed rotor fluxes enable the direct computation of the electrical position angle and a PLL may be eliminated. This simplification reduces the complexity of the control structure and improves system efficiency. The high-precision rotor flux estimation provided by the observer enables direct and reliable computation of the electrical position angle, which is crucial for

precise motor control. Experimental validations have been conducted to evaluate the performance of the proposed method under both no-load and load conditions. The experimental results have revealed that the proposed method achieved tiny position errors, with a maximum steady-state error of only 0.030 rad at no load and less than 0.025 rad at heavy load. Compared to conventional methods, which exhibit a maximum position error of up to 0.250 rad, the proposed method offers up to 90% improvement in position accuracy. These results demonstrate that the proposed method delivers superior performance in both steady-state and dynamic conditions, which makes it highly suitable for DTP-AFPMSM control, particularly in EV applications where precision, cost-effectiveness, and system reliability are most important.

Author Contributions

Anchen Yang: investigation, methodology, software, validation, visualization, writing – original draft. **Mingyao Lin:** funding acquisition, project administration, supervision, writing – review and editing. **Yixiang Tu:** investigation, validation, writing – review and editing. **Lun Jia:** writing – review and editing. **Keman Lin:** writing – review and editing. **Peng Wang:** writing – review and editing.

Acknowledgements

Conflicts of Interest

The authors declare no conflicts of interest.

Data Availability Statement

The data that support the findings of this study are available from the corresponding author upon reasonable request.

References

1. X. Wang, Z. Wang, M. He, Q. Zhou, X. Liu, and X. Meng, "Fault-Tolerant Control of Dual Three-Phase PMSM Drives With Minimized Copper Loss," *IEEE Transactions on Power Electronics* 36, no. 11 (2021): 12938–12953, https://doi.org/10.1109/tpel.2021.3076509.

2. Y. Ren and Z. Q. Zhu, "Reduction of Both Harmonic Current and Torque Ripple for Dual Three-Phase Permanent-Magnet Synchronous Machine Using Modified Switching-Table-Based Direct Torque Control," *IEEE Transactions on Industrial Electronics* 62, no. 11 (2015): 6671–6683, https://doi.org/10.1109/tie.2015.2448511.

3. S. Hu, Z. Liang, W. Zhang, and X. He, "Research on the Integration of Hybrid Energy Storage System and Dual Three-Phase PMSM Drive in EV," *IEEE Transactions on Industrial Electronics* 65, no. 8 (2018): 6602–6611, https://doi.org/10.1109/tie.2017.2752141.

4. K. Yu and Z. Wang, "Online Decoupled Multi-Parameter Identification of Dual Three-Phase IPMSM Under Position-Offset and HF Signal Injection," *IEEE Transactions on Industrial Electronics* 71, no. 4 (2024): 3429–3440, https://doi.org/10.1109/tie.2023.3273256.

5. Y. Hu, Z. Q. Zhu, and M. Odavic, "Comparison of Two-Individual Current Control and Vector Space Decomposition Control for Dual Three-Phase PMSM," *IEEE Transactions on Industry Applications* 53, no. 5 (2017): 4483–4492, https://doi.org/10.1109/tia.2017.2703682.

6. Z. Wang, K. Yu, Y. Li, and M. Gu, "Position Sensorless Control of Dual Three-Phase IPMSM Drives With High-Frequency Square-Wave Voltage Injection," *IEEE Transactions on Industrial Electronics* 70, no. 10 (2023): 9925–9934, https://doi.org/10.1109/tie.2022.3222683.

7. X. Qiu, J. Ji, D. Zhou, W. Zhao, Y. Chen, and L. Huang, "A Modified Flux Observer for Sensorless Direct Torque Control of Dual Three-Phase PMSM Considering Open-Circuit Fault," *IEEE Transactions on Power Electronics* 37, no. 12 (2022): 15356–15369, https://doi.org/10.1109/tpel.2022.3195495.

8. A. H. Almarhoon, Z. Q. Zhu, and P. Xu, "Improved Rotor Position Estimation Accuracy by Rotating Carrier Signal Injection Utilizing Zero-Sequence Carrier Voltage for Dual Three-Phase PMSM," *IEEE Transactions on Industrial Electronics* 64, no. 6 (2017): 4454–4462, https://doi.org/10.1109/tie.2016.2561261.

9. G. Wang, M. Valla, and J. Solsona, "Position Sensorless Permanent Magnet Synchronous Machine Drives—A Review," *IEEE Transactions on Industrial Electronics* 67, no. 7 (2020): 5830–5842, https://doi.org/10.1109/tie.2019.2955409.

10. S. Sul, Y. Kwon, and Y. Lee, "Sensorless Control of IPMSM for Last 10 Years and Next 5 Years," *CES Transactions on Electrical Machines and Systems* 1, no. 2 (2017): 91–99, https://doi.org/10.23919/tems.2017.7961290.

11. A. Yang, M. Lin, P. Cai, et al., "Position Identification Algorithm of PMSM Based on Improved Nonlinear TD Method," *IEEE Journal of Emerging and Selected Topics in Power Electronics* 13, no. 1 (2025): 564–575, https://doi.org/10.1109/jestpe.2024.3479461.

12. K. Lin, P. Wang, P. Cai, X. Wu, and M. Lin, "Fast Initial Rotor Position Estimation for IPMSM With Unipolar Sequence-Pulse Injection," *IEEE Transactions on Energy Conversion* 36, no. 4 (2021): 3545–3554, https://doi.org/10.1109/tec.2021.3087646.

13. P. Wang, Z. Q. Zhu, and D. Liang, "Virtual Signal Injection-Based Online Full-Parameter Estimation of Surface-Mounted PMSMs Without Influence of Position Error and Inverter Nonlinearity," *IEEE Journal of Emerging and Selected Topics in Power Electronics* 13, no. 2 (2025): 2341–2357, https://doi.org/10.1109/JESTPE.2025.3544820.

14. H. Wang, Y. Yang, X. Ge, Y. Zuo, Y. Yue, and S. Li, "PLL- and FLL-Based Speed Estimation Schemes for Speed-Sensorless Control of Induction Motor Drives: Review and New Attempts," *IEEE Transactions on Power Electronics* 37, no. 3 (2022): 3334–3356, https://doi.org/10.1109/tpel.2021.3117697.

15. X. Lu, H. Lin, and J. Han, "Load Disturbance Observer-Based Control Method for Sensorless PMSM Drive," *IET Electric Power Applications* 10, no. 8 (2016): 735–743, https://doi.org/10.1049/iet-epa.2015.0550.

16. W. Zhao, S. Jiao, Q. Chen, D. Xu, and J. Ji, "Sensorless Control of Linear Permanent-Magnet Machine Based on Improved Disturbance Observer," *IEEE Transactions on Industrial Electronics* 65, no. 12 (2018): 9291–9300, https://doi.org/10.1109/tie.2018.2823660.

17. Y. Park and S.-K. Sul, "Sensorless Control Method for PMSM Based on Frequency-Adaptive Disturbance Observer," *IEEE Journal of Emerging and Selected Topics in Power Electronics* 2, no. 2 (2014): 143–151.

18. T. H. Nguyen, T. T. Nguyen, V. Q. Nguyen, K. M. Le, H. N. Tran, and J. W. Jeon, "An Adaptive Sliding-Mode Controller With a Modified Reduced-Order Proportional Integral Observer for Speed Regulation of a Permanent Magnet Synchronous Motor," *IEEE Transactions on Industrial Electronics* 69, no. 7 (2022): 7181–7191, https://doi.org/10.1109/tie.2021.3102427.

19. H. Kim, J. Son, and J. Lee, "A High-Speed Sliding-Mode Observer for the Sensorless Speed Control of a PMSM," *IEEE Transactions on Industrial Electronics* 58, no. 9 (2011): 4069–4077, https://doi.org/10.1109/tie.2010.2098357.

20. M. S. Zaky, M. K. Metwaly, H. Z. Azazi, and S. A. Deraz, "A New Adaptive SMO for Speed Estimation of Sensorless Induction Motor

Drives at Zero and Very Low Frequencies," *IEEE Transactions on Industrial Electronics* 65, no. 9 (2018): 6901–6911.

21. Y. Zuo, C. Lai, and K. L. V. Iyer, "A Review of Sliding Mode Observer Based Sensorless Control Methods for PMSM Drive," *IEEE Transactions on Power Electronics* 38, no. 9 (2023): 11352–11367, https://doi.org/10.1109/tpel.2023.3287828.

22. I. Boldea, M. C. Paicu, G.-D. Andreescu, and F. Blaabjerg, "'Active Flux' DTFC-SVM Sensorless Control of IPMSM," *IEEE Transactions on Energy Conversion* 24, no. 2 (2009): 314–322, https://doi.org/10.1109/tec.2009.2016137.

23. I. Boldea, M. C. Paicu, and G.-D. Andreescu, "Active Flux Concept for Motion-Sensorless Unified AC Drives," *IEEE Transactions on Power Electronics* 23, no. 5 (2008): 2612–2618, https://doi.org/10.1109/tpel.2008.2002394.

24. W. Zhao, A. Yang, J. Ji, Q. Chen, and J. Zhu, "Modified Flux Linkage Observer for Sensorless Direct Thrust Force Control of Linear Vernier Permanent Magnet Motor," *IEEE Transactions on Power Electronics* 34, no. 8 (2019): 7800–7811, https://doi.org/10.1109/tpel.2018.2879411.

25. A. Yang, M. Lin, L. Jia, and K. Lin, "A Hall-Based Modified Finite Position Set-Phase Locked Loop for PMSM Control System in EVs," *IEEE Transactions on Applied Superconductivity* 34, no. 8 (2024): 1–5, https://doi.org/10.1109/tasc.2024.3456565.

26. X. Wu, D. Yang, S. Huang, et al., "Improved Rotor Flux Observer With Disturbance Rejection for Sensorless SPMSM Control," *IEEE Transactions on Transportation Electrification* 10, no. 2 (2024): 3603–3612, https://doi.org/10.1109/tte.2023.3308719.

27. G. Liang, W. Liao, Z. Zhang, et al., "An Optimized Pulsewidth Modulation for Dual Three-Phase PMSM Under Low Carrier Ratio," *IEEE Transactions on Power Electronics* 37, no. 3 (2022): 3062–3072, https://doi.org/10.1109/tpel.2021.3114304.

28. X. Bin, X. Luo, L. Zhu, and J. Zhao, "Sensorless Control of Dual Three-Phase PMSM With High Frequency Voltage Signal Injection," in *2019 22nd International Conference on Electrical Machines and Systems (ICEMS)* (2019), 1–4.

29. X. Zhang, Q. Xu, Y. Wang, Y. Miao, X. Wang, and F. Zhang, "Harmonic Current Suppression for Dual Three-Phase PMSM Based on Disturbance Observer," in *2023 26th International Conference on Electrical Machines and Systems (ICEMS)* (2023), 3099–3104.

30. G. Liang, S. Huang, W. Liao, et al., "An Optimized Modulation of Torque and Current Harmonics Suppression for Dual Three-Phase PMSM," *IEEE Transactions on Transportation Electrification* 10, no. 2 (2024): 3443–3454, https://doi.org/10.1109/tte.2023.3301971.